Available online at www.sciencedirect.com

ScienceDirect

Geochimica et Cosmochimica Acta 154 (2015) 49–65

Geochimica et Cosmochimica Acta

www.elsevier.com/locate/gca

Formation of iddingsite veins in the martian crust by centripetal replacement of olivine: Evidence from the nakhlite meteorite Lafayette

M.R. Lee [a,*], T. Tomkinson [a,b], L.J. Hallis [a], D.F. Mark [b]

[a] School of Geographical and Earth Sciences, University of Glasgow, Gregory Building, Lilybank Gardens, Glasgow G12 8QQ, UK
[b] Scottish Universitites Environmental Research Centre, Rankine Avenue, Scottish Enterprise Technology Park, East Kilbride G75 0QF, UK

Received 4 October 2014; accepted in revised form 9 January 2015; available online 28 January 2015

Abstract

The Lafayette meteorite is an olivine clinopyroxenite that crystallized on Mars ~1300 million years ago within a lava flow or shallow sill. Liquid water entered this igneous rock ~700 million years later to produce a suite of secondary minerals, collectively called 'iddingsite', that occur as veins within grains of augite and olivine. The deuterium/hydrogen ratio of water within these secondary minerals shows that the aqueous solutions were sourced from one or more near-surface reservoirs. Several petrographically distinct types of veins can be recognised by differences in their width, shape, and crystallographic orientation. Augite and olivine both contain veins of a very fine grained hydrous Fe- and Mg-rich silicate that are ~1–2 μm in width and lack any preferred crystallographic orientation. These narrow veins formed by cementation of pore spaces that had been opened by fracturing and probably in response to shock. The subset of olivine-hosted veins whose axes lie parallel to (0 0 1) have serrated walls, and formed by widening of the narrow veins by interface coupled dissolution–precipitation. Widening started by replacement of the walls of the narrow precursor veins by Fe–Mg silicate, and a crystallographic control on the trajectory of the dissolution–precipitation front created micrometre-scale {1 1 1} serrations. The walls of many of the finely serrated veins were subsequently replaced by siderite, and the solutions responsible for carbonation of olivine also partially recrystallized the Fe–Mg silicate. Smectite was the last mineral to form and grew by replacement of siderite. This mineralization sequence shows that Lafayette was exposed to two discrete pulses of aqueous solutions, the first of which formed the Fe–Mg silicate, and the second mediated replacement of vein walls by siderite and smectite. The similarity in size, shape and crystallographic orientation of iddingsite veins in the Lafayette meteorite and in terrestrial basalts demonstrates a common microstructural control on water–mineral interaction between Mars and Earth, and indicates that prior shock deformation was not a prerequisite for aqueous alteration of the martian crust.
© 2015 The Authors. Published by Elsevier Ltd. This is an open access article under the CC BY license (http://creativecommons.org/licenses/by/4.0/).

1. INTRODUCTION

The nakhlite meteorites are cumulate clinopyroxenites (Bunch and Reid, 1975; Friedman-Lentz et al., 1999; Treiman, 2005) that are believed to originate from the same igneous body on Mars, either a lava flow or shallow sill (Treiman, 1986; Friedman-Lentz et al., 1999; Mikouchi et al., 2006, 2012). This cogenetic model is supported by their common ages of crystallization (Amazonian, 1327 ± 39 Ma; Borg and Drake, 2005 and references therein) and ejection (~11 Ma; Eugster et al., 1997). These meteorites are potentially powerful tools for exploring the Amazonian hydrosphere of Mars because their parent igneous rock interacted with liquid water to form a suite

* Corresponding author.
E-mail address: Martin.Lee@Glasgow.ac.uk (M.R. Lee).

http://dx.doi.org/10.1016/j.gca.2015.01.022
0016-7037/© 2015 The Authors. Published by Elsevier Ltd.
This is an open access article under the CC BY license (http://creativecommons.org/licenses/by/4.0/).

of secondary minerals (e.g., Bunch and Reid, 1975; Bridges and Grady, 2000; Treiman, 2005). Owing to their fine grain size and intimate intermixture, these minerals are collectively termed 'iddingsite', but are known to include hydrous silicates, carbonates, sulphates, halides and oxides (Bunch and Reid, 1975; Reid and Bunch, 1975; Gooding et al., 1991; Treiman et al., 1993; Bridges and Grady, 2000). From a compilation of dates for secondary mineralization of the nakhlite meteorites Lafayette and Yamato 000593, Borg and Drake (2005) derived a weighted average age of 633 ± 23 Ma (i.e., Amazonian). They noted that this well-defined age implies a singular alteration event, possibly related to an impact or igneous activity. Here we have sought to understand better the drivers of interaction of liquid water with the nakhlite parent rock through characterisation of the microstructure of iddingsite veins within grains of augite and olivine. The Lafayette meteorite has been selected for study because it has the highest water content amongst the nakhlites (0.373–0.387 wt.%; Karlsson et al., 1992; Leshin et al., 1996), and its iddingsite veins are correspondingly the widest and most mineralogically diverse within the group (Changela and Bridges, 2011).

Specific questions concerning interactions between the martian crust and reservoirs of water (i.e., atmosphere, hydrosphere, cryosphere) that can be addressed using Lafayette iddingsite veins include: (i) the origin of solutes for the secondary minerals (e.g., derived solely from within augite and olivine grains by dissolution; sourced by dissolution of other parts of the nakhlite parent rock; derived from another region of the crust or the planet's surface); (ii) the longevity of solutions (e.g., a single short-lived episode of aqueous alteration *versus* multiple phases of fluid–rock interaction?); (iii) the petrophysical properties of the lava flow/sill (i.e., was impact fracturing a prerequisite for fluids to gain access to the igneous body, or was much of the space for secondary mineralization created by dissolution and/or replacement?). These questions will be answered by testing two hypotheses for vein formation, and the tests will use new observations of the petrofabric of Lafayette, the size, shape and crystallographic orientation of augite- and olivine-hosted veins, and the microstructure, stratigraphy and mineralogy of their fill. We also compare and contrast results from Lafayette with the microstructure of iddingsite veins in carbonaceous chondrite meteorites and terrestrial basalts.

The *cementation* hypothesis proposes that Lafayette olivine grains had a high density of open intra- and inter-granular fractures, likely as a consequence of shock deformation, and the secondary minerals formed mainly by cementation of these pore networks (Vicenzi and Heaney, 2000; Changela and Bridges, 2011; Bridges and Schwenzer, 2012; Hicks et al., 2014). A corollary of this model is that solutes must have been sourced externally to the grains that contain the iddingsite, and the secondary minerals would have filled the fractures by growing inwards from vein walls so that the last formed minerals will be on the vein axis. The *replacement* hypothesis (Reid and Bunch, 1975; Treiman et al., 1993; Meunier et al., 2012) envisages secondary minerals to have formed at the expense of their augite and olivine hosts and by coupled dissolution-precipitation. If replacement were centripetal (i.e., from the vein axis outwards, and thus from the margin of the unaltered reactant mineral towards its interior), as is typical for serpentinisation of terrestrial olivine (e.g., Delvigne et al., 1979; Velbel, 1984, 1993, 2012), the first formed minerals will be on the vein axis. Our initial study of aqueous alteration of Lafayette focused on the origin of siderite within grains of olivine and the intercumulate mesostasis as revealed by SEM imaging (Tomkinson et al., 2013a). Here we have built on this earlier work by investigating the mineralogy and nanoscale microstructure of iddingsite veins in augite and olivine grains using a suite of high resolution electron imaging and diffraction techniques.

2. MATERIALS, METHODS AND NOMENCLATURE

2.1. The Lafayette meteorite

Lafayette is a 0.8 kg stone that was first recognised as a meteorite in 1931 (Nininger, 1935). It was believed to have fallen in Indiana a few years prior to its recognition, but as Lafayette has a terrestrial age of 2900 ± 1000 years (Jull et al., 1999), the post-fall history of this meteorite remains unclear. Although it is therefore possible that the secondary minerals that have been investigated here are products of terrestrial weathering, a predominantly martian origin is indicated by the fact that they are cut by the fusion crust, and their $\Delta^{17}O$ and δD values have a martian signature (Karlsson et al., 1992; Treiman et al., 1993; Leshin et al., 1996; Tomkinson et al., 2013b). This study used a thin section of Lafayette (USNM 1505-5), which is semicircular and 10.3×8.3 mm in size (Fig. 1a), together with a polished block containing olivine grains that had been physically separated from bulk sample NHM1959 755.

2.2. Analytical methods

Backscattered electron (BSE) images and qualitative X-ray spot analyses were obtained from these samples after carbon coating and using two field-emission SEMs, both operated at 20 kV: a FEI Quanta 200F equipped with an EDAX Genesis energy-dispersive X-ray (EDX) analysis system, and a Zeiss Sigma equipped with an Oxford Instruments Aztec EDX analysis system. BSE contrast is proportional to mean atomic number (Z), and so these images reveal the presence of different minerals and compositional variations within them (e.g., zoning). The volumetric abundance of various constituents of the thin section was determined by point counting using the SEM with a step size scaled to the sizes of the features of interest. The density and orientation of fractures and veins within grains of augite and olivine was quantified by the following procedure. Eight lines were drawn onto an image of each grain in a star-shaped pattern (i.e., so that each line is rotated by 22.5° relative to its neighbour). The number of fractures and veins intersected by each line was counted, and this number was divided by the length of the line to give the fracture/vein density (i.e., fractures/veins μm^{-1}). The degree of preferred orientation of fractures and veins in each grain was expressed as the percentage difference

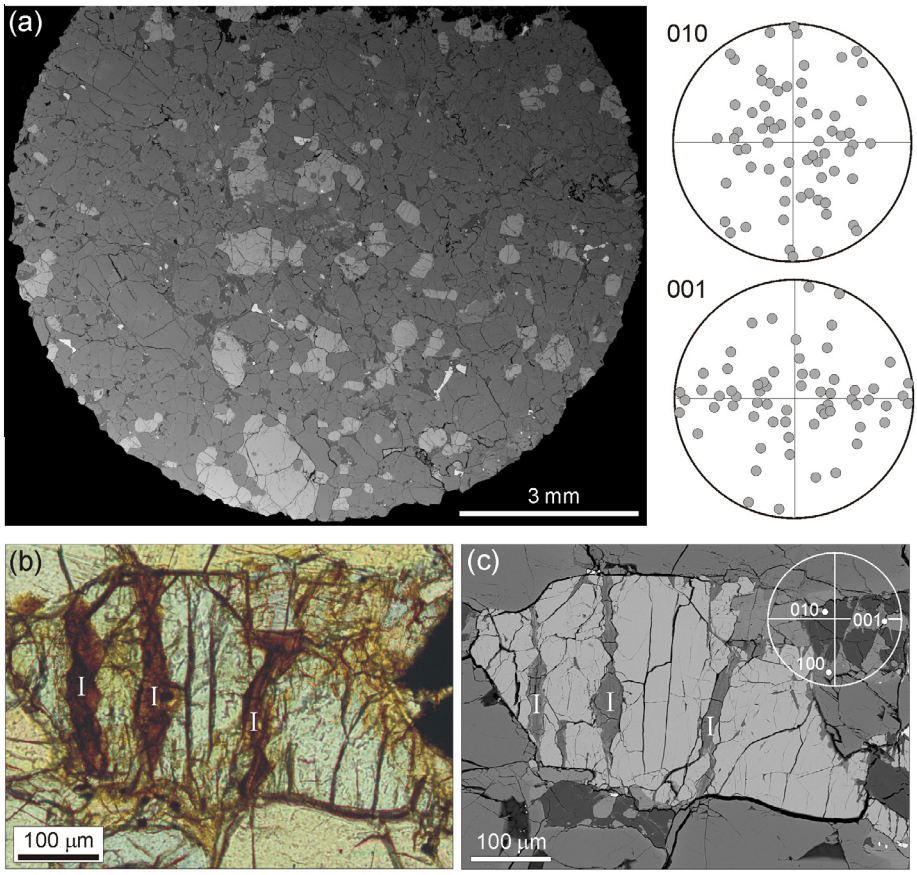

Fig. 1. (a) Backscattered electron (BSE) SEM image of the Lafayette thin section. Olivine grains are light grey, augite grains are mid-grey, and areas of mesostasis are dark grey. The small white grains are titanomagnetite. To the right hand side are EBSD pole figures showing the orientations of poles to (010) and (001) planes of 30 olivine grains plotted in both upper and lower hemispheres. Some of the olivine grains contain two crystals of different orientations. These pole figures show that the olivine crystals have a weak preferred orientation. (b) Plane polarised transmitted light image of one of the olivine grains. It contains three coarsely serrated veins of iddingsite (I) along with several fractures in the same orientation. (c) BSE image of the same field of view as (b). The inset EBSD upper hemisphere pole figure shows that the axes of the coarsely serrated iddingsite (I) veins are parallel to the trace of $(001)_{ol}$, as are some of the fractures. Note that the iddingsite veins stop abruptly at the $(100)_{ol}$-parallel olivine grain boundaries.

between lines with the lowest fracture/vein density (f_{min}/v_{min}) and the highest fracture/vein density (f_{max}/v_{max}). For example, a preferred orientation factor of 0% means that f_{min} is 0% of f_{max} (i.e., at least 1 of the 8 lines intersects no fractures), whereas a preferred orientation factor of 100% shows that $f_{min} = f_{max}$ (i.e., all 8 lines intersect the same number of fractures). A worked example is in Supplementary Fig. 1.

Electron backscatter diffraction (EBSD) was used to determine the crystallographic orientations of features within olivine grains, including grain boundaries, fractures, veins, and teeth and notches on serrated vein walls. EBSD work employed an EDAX-TSL system attached to the Quanta SEM running OIM software. Mapping was undertaken after removal of the carbon coat and following a brief polish in colloidal silica. The SEM was operated at 20 kV, using a moderately high beam current (not quantified by this SEM), and in low vacuum mode (~50 Pa). Kikuchi patterns were acquired at a rate of ~20 to 40 s^{-1} and with a ~0.1 μm step size. Orientation data are plotted in stereographic pole figures, either in the upper hemisphere only or both hemispheres. Transmission electron microscope (TEM) imaging and selected area electron diffraction (SAED) was used to study the microstructures of olivine grains (e.g., dislocations and subgrain boundaries) and the constituents of olivine-hosted secondary mineral veins. Electron transparent foils for TEM work were cut and extracted from olivine crystals in the grain mount using a FEI DuoMill focused ion beam (FIB) instrument and following the procedure of Lee et al. (2003). Milling was undertaken using 30 kV Ga^+ ions; each foil was initially milled to a thickness of ~1 μm, then was lifted out using an *in-situ* micromanipulator, welded to the tine of a Cu support and further 'polished' to ~90 to 100 nm at lower beam current. Initial imaging of the foils was by low voltage scanning transmission electron microscopy (LV-STEM; Lee and Smith, 2006), using the Zeiss Sigma SEM operated at 20 kV/1 nA. This technique was also used for qualitative chemical analysis, with X-ray spectra being acquired via the Aztec system. The foils were then mounted in a double-tilt holder and examined using a FEI T20 TEM operated at 200 kV. Contrast in bright-field images is due to

spatial variations in the degree of electron scattering, and as the foils are essentially parallel sided (i.e., equal thickness throughout), scattering intensity will vary with Z and the orientation of crystalline regions relative to the electron beam (i.e., Bragg scattering; Lee, 2010). SAED patterns were acquired using a ~1 μm diameter selected area aperture, and the aggregate of measurement and camera factor *d*-spacing errors are ~1% of *d*-spacing values. High angle annular dark-field (HAADF) images of the foils were obtained using a JEOL MagTEM aberration-corrected field-emission instrument operated at 200 kV and in STEM mode. The high energy ion and electron beams used in the FIB and TEM work have the potential to damage the crystalline structure and chemical composition of the vein constituents, especially given their likely hydrous composition (Lee et al., 2007). Although we have sought to minimise the potential for such damage, we have been cautious in our interpretation of the original crystallinity of those vein constituents that are shown by TEM to be poorly crystalline or amorphous.

2.3. Terminology used for Lafayette secondary minerals

Iddingsite occurs as veins within augite and olivine grains (Fig. 1b, c), and as patches within the mesostasis. The focus of the present study is on elucidating vein origins using their microstructure, because the mineralogy of their fill has been the subject of several previous studies. This earlier work has shown that the veins have four main constituents. All veins contain a narrow band of a hydrous silicate that is rich in Fe and Mg. This Fe–Mg silicate was first analysed in detail by Treiman et al. (1993), who concluded from the results of X-ray microanalysis (Table 1) together with TEM imaging and SAED that it is composed of <20 nm sized crystallites of trioctahedral ferrous saponite together with Si- and S-bearing ferrihydrite and magnetite. By contrast, Changela and Bridges (2011) also used TEM to find that it is an 'amorphous gel'. Given these differences in interpretation, this material is referred to as *Fe–Mg silicate*, although some new observations pertaining to its mineralogy and crystallinity are described. *Fibrous phyllosilicate* occurs in all of the wider olivine-hosted veins. Treiman et al. (1993) described it as 'coarse grained phyllosilicate', and found that it is composed of ~1 μm sized crystals, often arranged in radiating sprays, whose chemical composition and ~1 nm lattice fringe spacing are consistent with a ferroan smectite. Changela and Bridges (2011) supported the interpretation of Treiman et al. (1993), but suggested that serpentine may also be present. Hicks et al. (2014) found that the fibrous phyllosilicate is a ferric saponite. Between Fe–Mg silicate and fibrous phyllosilicate of many of the olivine-hosted veins is a selvage of a material that has a higher Z than its surroundings. It was described as *porous oxide* by Treiman et al. (1993), who concluded

Table 1
Chemical compositions of primary and secondary constituents of the Lafayette meteorite.

	Olivine core[a]	Augite core[a]	Plagioclase[b]	Fe–Mg silicate, high Z[c]	Fe–Mg silicate, low Z[c]	Porous oxide[c]
SiO_2	31.94	51.36	60.7	49.5	50.3	3.96
TiO_2	n/a	0.23	n/a	0.01	0.01	0.00
Al_2O_3	n/a	0.85	23.5	4.48	4.16	1.38
Cr_2O_3	n/a	0.39	n/a	0.00	0.00	0.00
FeO	52.09	14.12	0.83	29.02	27.82	77.1
NiO	0.03	n/a	n/a	0.01	0.09	0.14
MnO	0.97	0.41	n/a	0.49	0.49	2.58
MgO	13.41	12.79	0.10	13.61	14.45	4.30
CaO	0.19	18.50	7.1	0.72	0.75	0.70
Na_2O	n/a	0.21	7.3	0.33	0.30	0.00
K_2O	n/a	n/a	0.71	0.35	0.38	0.03
P_2O_5	n/a	n/a	0.00	0.09	0.09	0.65
SO_3	n/a	n/a	n/a	0.81	0.83	8.78
Cl	n/a	n/a	n/a	0.45	0.39	0.36
Total	98.63	98.87	100.24	99.87	100.06	99.98
n	18	18	1	30	23	2
Major element ratios						
Al/Si	——	0.02	0.44	0.10	0.09	0.39
Fe/Si	2.71	0.46	0.02	0.97	0.92	32.38
Mn/Si	0.05	0.01	——	0.02	0.02	1.08
Mg/Si	0.54	0.32	——	0.35	0.37	1.40
Ca/Si	0.01	0.55	0.18	0.02	0.02	0.27
Mg/Fe	0.20	0.70	0.09	0.36	0.40	0.04

n denotes number of analyses.
n/a denotes not analysed.
—— denotes not applicable.
[a] EPMA data in Harvey and McSween (1992).
[b] EPMA data in Bunch and Reid (1975).
[c] SEM-EDX data in Treiman et al. (1993), which were normalised on an anhydrous basis. The high Z Fe–Mg silicate and low Z Fe–Mg silicate were referred to by Treiman et al. (1993) as bright fine veins and dark fine veins respectively.

from TEM imaging and X-ray microanalysis (Table 1) that it is composed of sub-micrometre sized crystals of magnetite or maghemite; Changela and Bridges (2011) suggested that it contains ferrihydrite. We provide new observations regarding the mineralogy of this material, and interpretations of its origin, but for consistency retain the original 'porous oxide' nomenclature of Treiman et al. (1993). *Siderite* was first described from Lafayette iddingsite veins by Vicenzi et al. (1997), who recorded a composition of $Fe_{63.4\text{-}67.4}Mn_{7.7\text{-}10.6}Ca_{26.2\text{-}25.2}Mg_{0.2\text{-}0.3}CO_3$.

3. RESULTS

3.1. Mineralogy of Lafayette

The thin section (Fig. 1a) contains 75.5 vol.% augite, 12.8 vol.% olivine, 6.8 vol.% mesostasis, 3.6 vol.% iddingsite, 1.3 vol.% orthopyroxene, and 0.9 vol.% Fe–Ti oxide (data from SEM point counting; $n = 470$ points excluding porosity). Pore space principally consists of fractures up to 10 μm wide that are present along most grain boundaries, together with fractures less than 5 μm in width that cross-cut mineral grains and the mesostasis. As discussed below, petrographic evidence shows that some of these fractures predate the precipitation of secondary minerals, whereas others must have formed after aqueous activity because they cross-cut the veins.

Augite occurs as 0.2–1.0 mm sized equant to tabular crystals that have a compositionally uniform core ($En_{37}Fs_{24}Wo_{39}$, Harvey and McSween, 1992; Table 1) and a ~15 μm wide rim that relative to the core is depleted in Mg and enriched in Fe. The edges of crystals occasionally have overgrowths of low-Ca pyroxene that contain submicrometre wide exsolution lamellae of augite. Olivine grains are 0.13–1.85 mm in size, have a mean composition of Fa_{69} (Harvey and McSween, 1992; Table 1), and EBSD mapping shows that the majority are single crystals. They range from equant to tabular in shape, and the long edges of tabular crystals usually lie parallel to the traces of $(1\,0\,0)_{ol}$ or $(0\,1\,0)_{ol}$. (Fig. 1c). EBSD also demonstrates that olivine crystals have a weak preferred orientation that defines a petrofabric (Fig. 1a) comparable to that recognised by Berkley et al. (1980) from the optically determined orientations of Lafayette augite crystals. Areas of mesostasis are ~100 to 600 μm across (Fig. 1a) and are dominated either by plagioclase feldspar ($Ab_{62.6}An_{31.8}Or_{5.6}$; Bunch and Reid, 1975; Table 1) or phyllosilicate that is often intergrown with siderite (Tomkinson et al., 2013a). The presence of secondary minerals within the mesostasis gives it a light brown colour when viewed using plane polarised transmitted light. Meunier et al. (2012) interpreted the phyllosilicate-rich mesostasis to be a precipitate from late-stage magmatic fluids, whereas Tomkinson et al. (2013a) concluded that phyllosilicate and siderite had formed by the water-mediated replacement of plagioclase feldspar.

3.2. Augite-hosted fractures and veins

All augite grains contain straight or curved sub-micrometre wide fractures (Fig. 2a) and the mean abundance of fractures per grain ranges from 0.016 to 0.022 μm^{-1}. The majority of them cross-cut entire grains, and these fractures have a weak to moderate preferred orientation of between 26% and 64% (Table 2). Some of the augite grains contain veins that are distinguished from fractures by their light brown colour in plane polarised transmitted light, and this colouration is especially noticeable where the vein is oriented at a low angle to the surface of the thin section (Fig. 2a). Vein walls are occasionally finely serrated, with notches up to ~0.4 μm deep (Fig. 2b, c). The veins contain a ~1 μm wide film of a material that is internally featureless in BSE images, has a lower Z than the host pyroxene, and whose qualitative chemical composition is consistent with the Fe–Mg silicate (Fig. 2b–d). Where augite and olivine grains are in contact, an augite-hosted vein may line up with the axis of an olivine-hosted iddingsite vein, and Fe–Mg silicate is continuous between the two (Fig. 2d). Veins in one augite grain have a density of 0.007 μm^{-1} and a weak preferred orientation of 38% (Table 2).

3.3. Olivine-hosted fractures and veins

The mean abundance of fractures and veins in olivine grains ranges from 0.016 to 0.036 μm^{-1} and from 0.006 to 0.013 μm^{-1}, respectively (Table 2). The fracture density of olivine is greater than that of augite, although many of the olivine-hosted fractures are sinuous and discontinuous, which is a type that is absent from the augite. Veins always have a much stronger preferred orientation than fractures in the same grain (Table 2). TEM shows that olivine has ~10^8 dislocations cm^{-2}, and in Fig. 3a these defects are oriented parallel to the trace of $(0\,1\,0)_{ol}$, and $[0\,0\,1]_{ol}$. Such properties are consistent with screw dislocations with a [0 0 1] Burgers vector on the (0 1 0) glide plane, and are characteristic of high strain rate/low temperature (<800 °C) deformation of olivine (Ashworth and Barber, 1975; Langenhorst et al., 1975, 1999). Point counting of two olivine grains shows that the iddingsite veins comprise 17.9 vol.% ($n = 160$ points in a 0.27 mm sized grain) and 21.3 vol.% ($n = 244$ points in a 0.13 mm sized grain). Given that the thin section contains 12.8 vol.% olivine, the overall abundance of olivine-hosted secondary mineral veins in Lafayette is 2.3–2.7 vol.%. Two vein types can be recognised by differences in their microstructure: (i) narrow parallel-sided veins (hereafter 'simple veins'), and (ii) wider veins with serrated walls (hereafter 'serrated veins'). Very few of either type of vein extend beyond olivine grain margins (Fig. 1b, c).

3.3.1. Microstructure and fill of the simple olivine-hosted veins

Simple veins are up to ~1 μm in width and may cross-cut entire grains or terminate within them (the latter are hereafter referred to as 'discontinuous' veins). They may intersect serrated veins, but never cross-cut them (Fig. 3b). Simple veins have a range of crystallographic orientations, but none occur with their axis near to $(0\,0\,1)_{ol}$, and a curved simple vein will pass into a serrated vein as its axis approaches $(0\,0\,1)_{ol}$. Simple veins contain only Fe–Mg silicate (Fig. 3b).

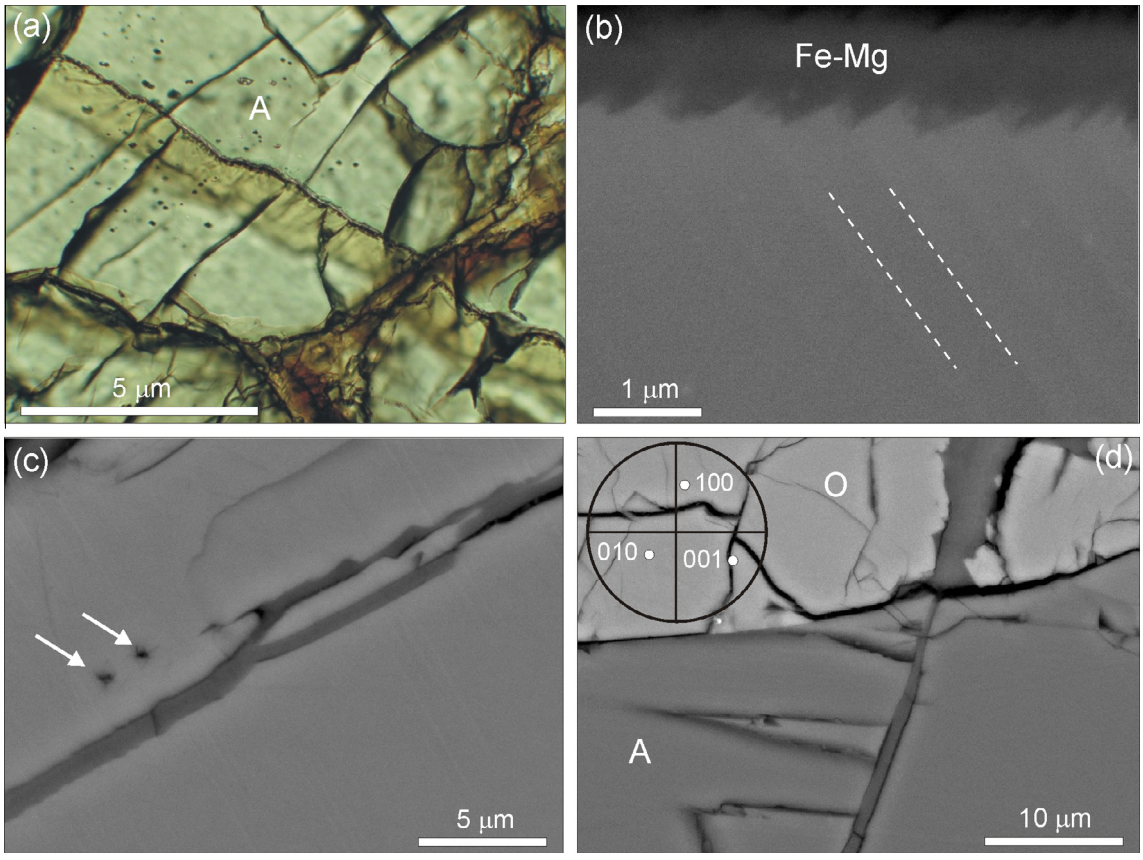

Fig. 2. (a) Plane polarised transmitted light image of an augite (A) grain containing a Fe–Mg silicate vein that extends from upper left to lower right. The grain also contains fractures in several different orientations. (b) BSE image of a Fe–Mg silicate vein (Fe–Mg) within low-Ca pyroxene. Fine serrations of the vein wall correspond to the thin augite exsolution lamellae (the edges of one are highlighted by dashed white lines). (c) BSE image of a pair of Fe–Mg silicate veins (dark grey) within augite. Most parts of these veins have planar walls, but the upper vein has serrated walls, and passes into a pair of sub-micrometre sized pores at its lower left hand end (arrowed). (d) BSE image of a vein of Fe–Mg silicate (dark grey) within augite (A) that is in-line with the axis of a much wider and finely serrated olivine (O)-hosted vein. The inset EBSD upper hemisphere pole figure shows that the axis of the olivine-hosted vein is parallel to the trace of $(0\,0\,1)_{ol}$.

Table 2
The density and orientation preference of fractures and veins in grains of augite and olivine.

	Number of fractures μm^{-1}			Fracture preferred orientation factor (%)	Number of veins μm^{-1}			Vein preferred orientation factor (%)
	f_{min}	f_{max}	f_{mean}		v_{min}	v_{max}	v_{mean}	
Augite grain 1	0.012	0.019	0.016	64	0.003	0.009	0.007	38
Augite grain 2	0.008	0.032	0.017	26	0	0	0	n/a
Augite grain 3	0.013	0.027	0.018	48	0	0	0	n/a
Augite grain 4	0.016	0.030	0.020	52	0	0	0	n/a
Augite grain 5	0.014	0.026	0.022	51	0	0	0	n/a
Olivine grain 1	0.007	0.028	0.016	25	0.000	0.026	0.013	0
Olivine grain 2	0.020	0.038	0.026	52	0.003	0.010	0.007	31
Olivine grain 3	0.018	0.043	0.027	41	0.005	0.019	0.010	25
Olivine grain 4	0.020	0.053	0.036	37	0.000	0.010	0.006	0
Olivine grain 5	0.025	0.052	0.035	47	0.000	0.019	0.011	0

The preferred orientation factor is calculated as $(100/f_{max}$ or $v_{max}) \times f_{max}$ or v_{min}.

3.3.2. Microstructure of the serrated olivine-hosted veins

Tomkinson et al. (2013a) recognised two types of serrated vein that differ in their width and in the wavelength and amplitude of their serrations: 'finely serrated' and 'coarsely serrated'. The central axis of both types of serrated vein lies parallel or at a low angle to the trace of $(0\,0\,1)_{ol}$ (e.g., Figs. 1c and 3c, d). Owing to this preferred crystallographic orientation, the observed width of a

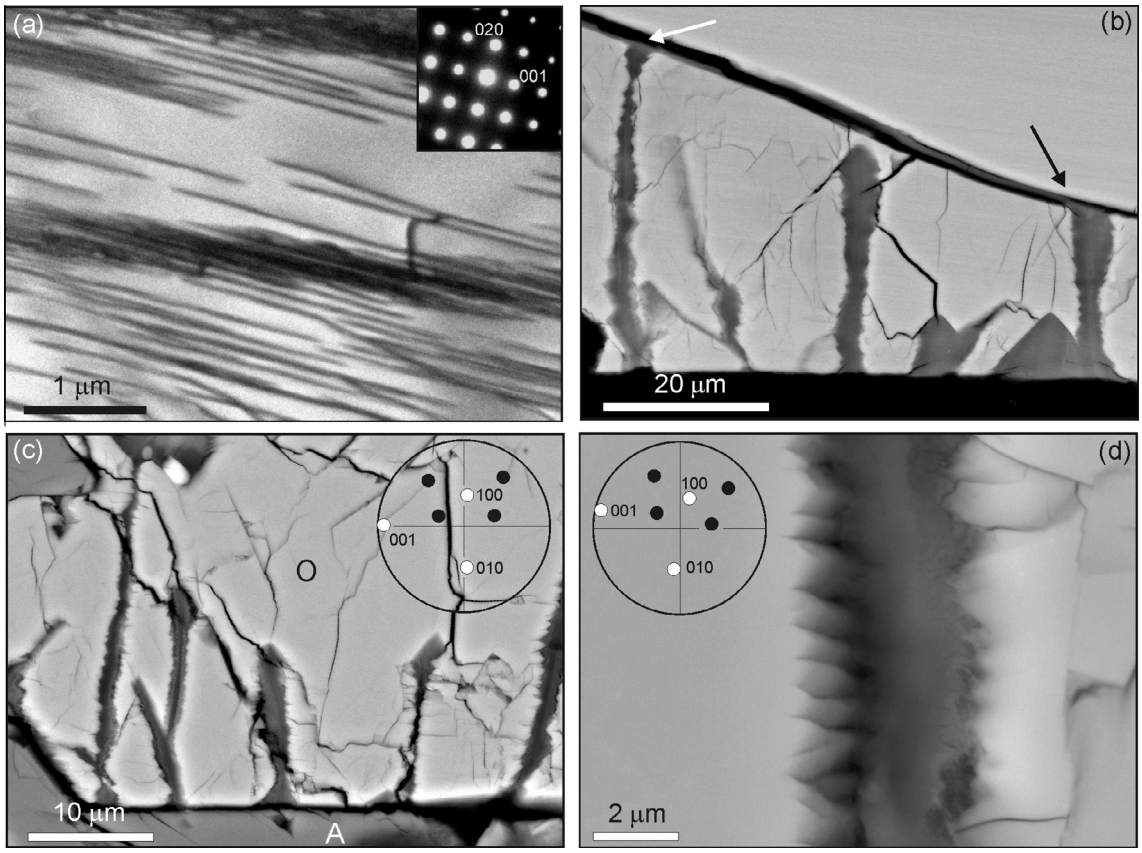

Fig. 3. (a) Bright-field TEM image of dislocations in the interior of an olivine grain. They have a density of $\sim 10^8$ cm^{-2}, and the inset [100] SAED pattern shows that they are oriented parallel to the trace of $(010)_{ol}$ and $[001]_{ol}$. (b) BSE image of the edge of an olivine grain that hosts both finely and coarsely serrated veins. Two of the serrated veins terminate at a curved simple vein into which their Fe–Mg silicate extends (arrowed). (c) Finely serrated veins extending from the boundary between an olivine (O) and augite (A) grain. The inset EBSD upper hemisphere pole figure shows that the grain boundary is parallel to the traces of both $(100)_{ol}$ and $(010)_{ol}$, and vein axes are parallel to the trace of $(001)_{ol}$. Poles to $\{111\}_{ol}$ planes are plotted in the black points. (d) A finely serrated vein whose Fe–Mg silicate fill (dark grey) has been partially lost during polishing to expose a vein wall. The image shows that the teeth seen at the polished grain surface are cross-sections of ridges whose apices are parallel to $(010)_{ol}$, as shown by the inset EBSD upper hemisphere pole figure (poles to {111} planes are plotted in the black points).

serrated vein will depend on the orientation of its host olivine grain relative to the surface of the thin section. The true width of a vein will be recorded only where the polished surface of its host grain is parallel to $[001]_{ol}$, and the observed vein width will increase in proportion to the angle between the polished surface and $[001]_{ol}$. Olivine grains whose polished surface is parallel to $[001]_{ol}$ plot around the circumference of the (001) pole figure in Fig. 1a, and veins in these grains range in width from 0.9 to 59.6 μm (mean = 13.2 μm, $n = 52$; Table 3).

Finely serrated veins may cross-cut grains, but are more commonly discontinuous and extend only ~10 to 30 μm into the interior of an olivine grain from $(100)_{ol}$ or $(010)_{ol}$ grain boundaries (Fig. 3b, c). They may terminate against simple veins (Fig. 3b) or cross-cut open fractures so that their secondary minerals span the fractures intact, thus indicating that the vein fill postdates the fracture. In olivine grains whose polished surface is near-parallel to $[001]_{ol}$ the serrations have an amplitude of ~0.2 to 0.7 μm, and a wavelength of~0.5 to 0.9 μm. The outline of the teeth is commonly delineated by the traces of $\{111\}_{ol}$ planes (Fig. 3c). Where the three-dimensional shape of $(001)_{ol}$ vein walls is revealed by partial loss of Fe–Mg silicate, the teeth are seen to have the shape of 'ridges' (Fig. 3d) or less commonly discrete 'pinnacles'. Hairline fractures extend 1–2 μm into olivine from the apices of the notches in vein walls. The tips of discontinuous

Table 3
The widths of veins in 6 grains of olivine.

Grain	Widths of individual veins			n
	Maximum	Minimum	Mean (1σ)	
1	14.7	1.1	4.6 (4.1)	14
2	12.9	0.9	5.5 (4.9)	5
3	25.3	5.0	16.3 (7.3)	6
4	56.2	1.4	16.4 (16.4)	11
5	30.1	5.5	16.9 (9.1)	9
6	59.6	3.4	23.5 (17.5)	7

The polished surface of all 6 grains was oriented close to [001]. Each vein was measured parallel to $[001]_{ol}$ and in its widest part. n denotes number of veins in each vein that were measured.

finely serrated veins have an 'arrowhead' shape that is defined by $\{111\}_{ol}$ and may pass into a 'train' of submicrometre sized inclusions that are in line with the vein axis and may also have a $\{111\}_{ol}$ habit (Fig. 4a); the fill of these 'faceted inclusions' is described below. Finely serrated veins may pass into coarsely serrated veins, and occasionally one wall of a vein is finely serrated and the other is coarsely serrated.

Coarsely serrated veins can cross-cut entire grains or may be discontinuous, and most are widest in the vicinity of $(100)_{ol}$ or $(010)_{ol}$ grain boundaries. There is no consistent relationship between the pattern of teeth and notches on opposite vein walls, and it is rare that they are arranged such that teeth on one wall would interlock with notches of the opposite wall if the vein were to close (e.g., Fig. 1c). In common with the finely serrated veins, some of the discontinuous coarsely serrated veins terminate against simple veins, whereas others pass into lines of faceted inclusions of secondary minerals (Fig. 4b). A foil cut through a faceted inclusion 13 μm beyond the tip of a coarsely serrated vein shows that its walls are crystallographically controlled, and the apex of one of the notches lines up precisely with a low angle subgrain boundary that is oriented parallel to the trace of $(001)_{ol}$ (Fig. 4c, d).

3.3.3. Fill of the serrated veins

All of the serrated veins contain Fe–Mg silicate, and it is the sole constituent of the narrowest finely serrated veins (Fig. 3b–d). Wider veins have an axial band of Fe–Mg silicate, which is typically 1–2 μm across in grain interiors, broadening to ~5 μm at their edges (Fig. 5a, c). This axial band is straddled by fibrous phyllosilicate with or without

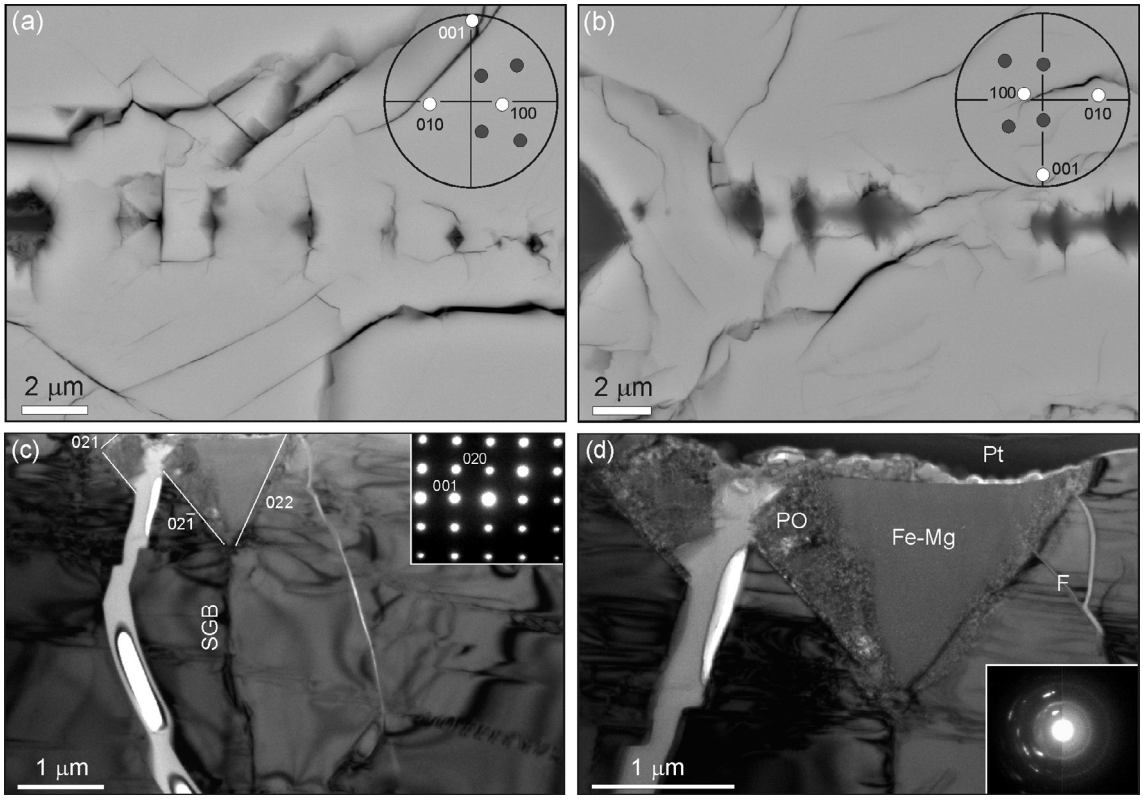

Fig. 4. (a) and (b) are BSE images of trains of faceted inclusions of Fe–Mg silicate that extend from the tips of serrated olivine-hosted veins. Plotted in the inset EBSD upper hemisphere pole figures are poles to the major planes; the {111} poles are the unlabeled black points. In (a) a train of inclusions extends parallel to the trace of $(001)_{ol}$ from the tip of a finely serrated vein (at the left hand edge of the image). The outlines of the two inclusions on the right hand side of the train are defined by $\{111\}_{ol}$. Hairline fractures extend into olivine from corners of these inclusions. (b) A train of faceted inclusions that lies parallel to the trace of $(001)_{ol}$ and runs between two coarsely serrated veins, whose tips are on the left and right hand edges of the image. Hairline fractures extend from the inclusions into olivine and parallel to the traces of $(100)_{ol}$ and $(010)_{ol}$. (c) and (d) are bright-field TEM images of a foil cut through a faceted inclusion 13 μm beyond the tip of a coarsely serrated olivine-hosted vein. The olivine grain contains a prominent subgrain boundary (SGB), and the [100] SAED pattern in (c) shows that the SGB lies parallel to the trace of $(001)_{ol}$. The walls of the faceted inclusion (highlighted by white lines), are crystallographically controlled as indicated. The apex of the inclusion intersects the SGB, and its left hand edge has been displaced along a fracture that is partly resin-filled (light grey). The oval shaped white area within the fracture is a hole. (d) The faceted inclusion contains Fe–Mg silicate (Fe–Mg), which has an irregular interface with porous oxide (PO) in its left hand part. A fracture (F) can be traced from the olivine into the faceted inclusion, but it is less well defined within the Fe–Mg silicate. The right hand part of the SAED pattern in (d) is from Fe–Mg silicate and the left hand part is from the porous oxide. The Fe–Mg silicate produces two rings (d-spacing 0.256 and 0.155 nm), and in the porous oxide these two rings are accompanied by spots, the innermost of which has a d-spacing of ~0.371 nm that is probably attributable to hematite $\{01\bar{1}2\}$ ($d = 0.369$ nm). The fracture that contains resin (light grey) and a elongate hole (white) is on the left hand side of the image.

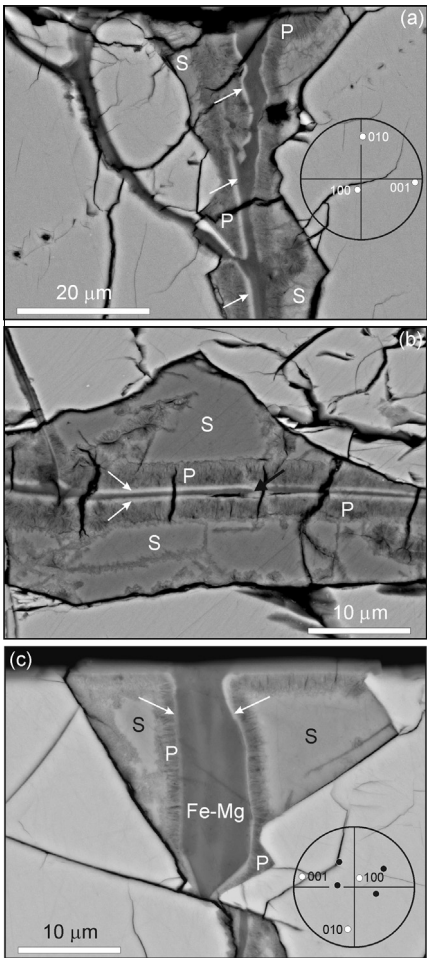

Fig. 5. BSE images of coarsely serrated veins that contain Fe–Mg silicate (Fe–Mg), porous oxide (narrow white bands indicated by white arrows), fibrous phyllosilicate (P) and siderite (S). The inset EBSD upper hemisphere pole figures show the orientation of poles to major planes. (a) A vein close to a grain boundary that is intersected by a curved simple vein on its left hand side. The coarsely serrated vein has an axial band of Fe–Mg silicate that is straddled by selvages of porous oxide. Beyond this is fibrous phyllosilicate, with siderite present in the deeper notches. The axis of the coarsely serrated vein is normal to the $(010)_{ol}$ grain boundary and parallel to the trace of $(001)_{ol}$. In the lower part of the vein the contact between Fe–Mg silicate and fibrous phyllosilicate is planar, whereas it is serrated close to the grain boundary. (b) A vein with an axial band of Fe–Mg silicate that is straddled by porous oxide and fibrous phyllosilicate. The rest of the vein comprises siderite that contains veinlets and rosettes of fibrous phyllosilicate. Note that the Fe–Mg silicate band is straight despite the irregularity of the olivine vein walls. A simple vein intersects the coarsely serrated vein (left hand side of the image), and Fe–Mg silicate, porous oxide and fibrous phyllosilicate are continuous between the two. A porous oxide veinlet cross-cuts the Fe–Mg silicate (indicated by the black arrow). This vein was also illustrated in Leshin and Vicenzi (2006). (c) A vein extending into olivine from a (010) grain boundary (along the top edge of the image). The vein axis lies close to the trace of $(001)_{ol}$, and its walls are parallel to traces of $\{111\}_{ol}$ (poles to $\{111\}$ planes are indicated by black points). It contains Fe–Mg silicate, which is straddled by selvages of porous oxide and 1.5 μm wide bands of fibrous phyllosilicate, and siderite is present within the notches.

porous oxide and siderite (Fig. 5). Where a simple vein intersects a serrated vein, Fe–Mg silicate is continuous between them (Figs. 3b and 5a, b).

The Fe–Mg silicate band may contain layers that are recognised in BSE images by differences in Z (Figs. 6 and 7), with the central layer typically having a higher Z than flanking layers (Fig. 6). A foil cut from one such band of Fe–Mg silicate shows that it contains 5 layers (Fig. 7a, b). Contrast differences between layers in the bright-field TEM image of the foil correspond to variations in the intensity of electron scattering, and so also Z. Qualitative

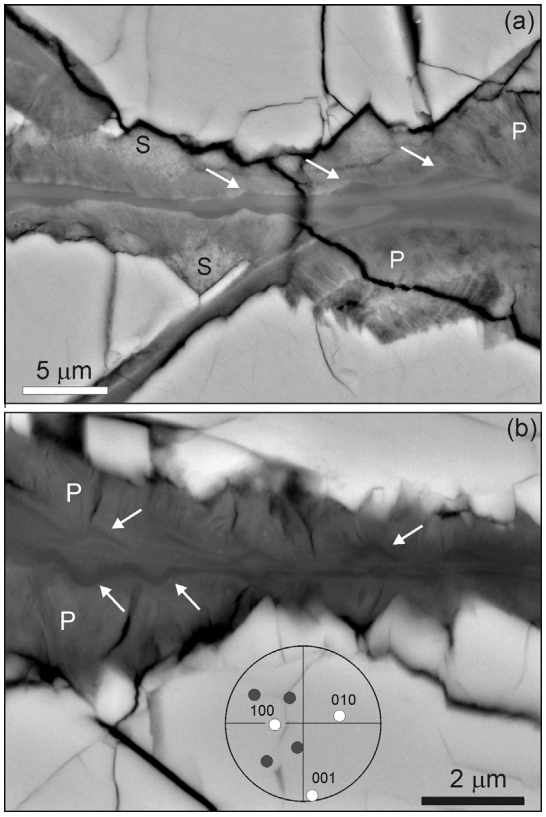

Fig. 6. BSE images of serrated olivine-hosted veins. Axial Fe–Mg silicate of both veins is flanked by fibrous phyllosilicate (P). Some of the phyllosilicate close to vein walls contains altered siderite (S). (a) A coarsely serrated vein containing two generations of Fe–Mg silicate. The central generation is light grey (i.e., higher Z) and parallel sided. It is flanked by a second generation that is darker grey, reflecting its lower Z, and has a serrated contact with the fibrous phyllosilicate (several of the notches are arrowed). A simple vein intersects the serrated vein along its lower edge. Its high-Z Fe–Mg silicate forms an angled layer within the fill of the coarsely serrated vein, but does not meet its central layer of high-Z Fe–Mg silicate. (b) A finely serrated vein containing axial Fe–Mg silicate that is flanked by fibrous phyllosilicate (P). The inset EBSD pattern shows that the shapes of the teeth and notches are defined by the traces of $\{111\}$ planes (poles to these planes are shown in the unlabelled grey symbols) and the vein axis is parallel to the trace of (001). The interface between Fe–Mg silicate and fibrous phyllosilicate is finely serrated, and the teeth and notches of these serrations, some of which are arrowed, are parallel to the traces of $\{111\}_{ol}$.

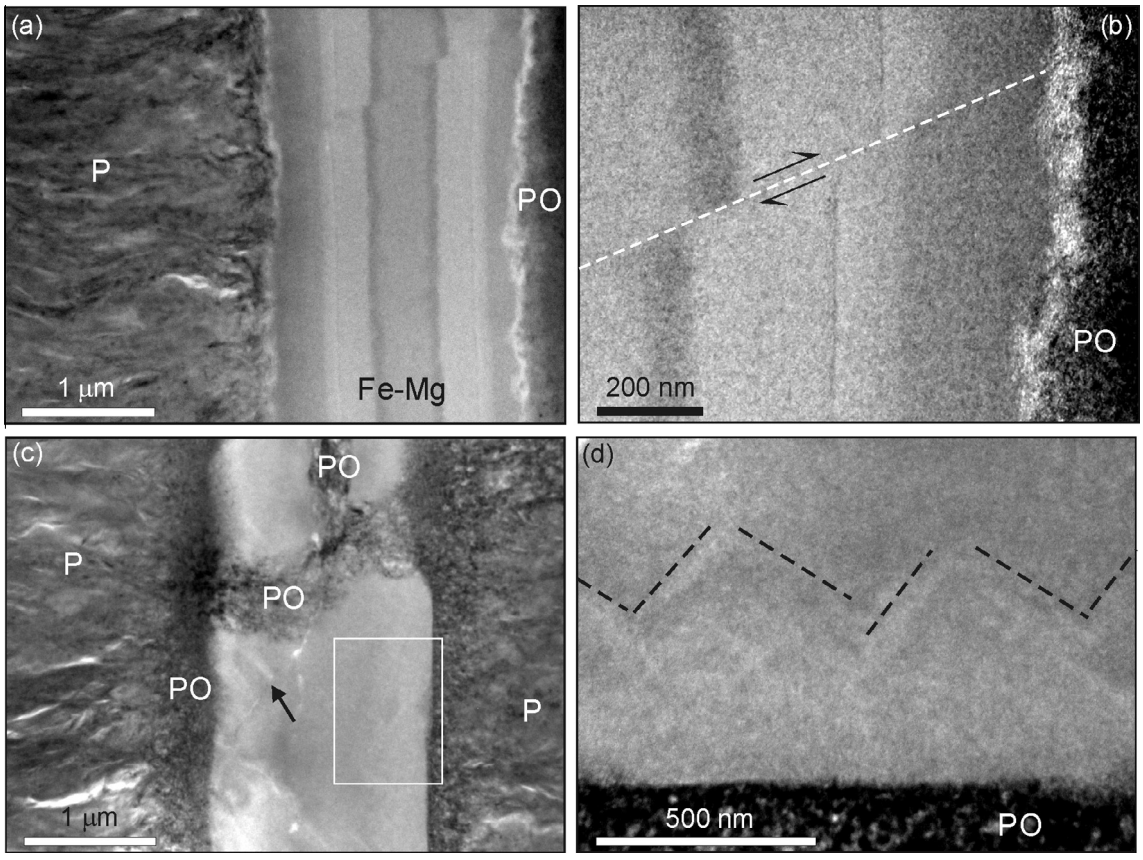

Fig. 7. Bright-field TEM images of Fe–Mg silicate (Fe–Mg), porous oxide (PO) and fibrous phyllosilicate (P) within coarsely serrated veins. (a) A layered band of Fe–Mg silicate that is straddled by porous oxide and fibrous phyllosilicate. The 5 layers are distinguished by differences in scattering intensity, which reflect contrasts in Z (principally Mg/Fe ratio). The dark layer on the right hand edge has an irregular contact with porous oxide so that its thickness varies. In the upper part of the image a fault displaces the layers by ~200 nm, but does not cut the fibrous phyllosilicate. (b) The right hand side of the fault in (a). The plane of movement is indicated by a dashed white line, and black arrows show the sense of displacement. As the fault does not cross-cut the porous oxide, brittle deformation of the Fe–Mg silicate must have predated formation of the porous oxide. (c) Image of a foil that was cut from a vein that was identified in BSE images as containing a selvage of porous oxide along the central axis of the Fe–Mg silicate band. The Fe–Mg silicate is straddled by porous oxide and fibrous phyllosilicate. Both edges of the Fe–Mg silicate band contain faint serrations that are visible owing to Z-related differences in the intensity of electron scattering; a serration on the left hand side is indicated by an arrow, and those serrations on the right hand side that are within the area indicated by the white rectangle are shown enlarged in (d). The Fe–Mg silicate is cross-cut by a sinuous vein of porous oxide that is continuous with the selvage of porous oxide lying on the vein axis. (d) Fe–Mg silicate on the right hand edge of the vein in (c) (note the image has been rotated 90° clockwise). Differences in grey scale (i.e., Z) highlight fine-scale serrations (delineated by the bashed black lines) whose teeth project towards the vein interior from the porous oxide wall.

EDX analysis confirms that these layers differ significantly in their Mg/Fe ratio, and Treiman et al. (1993) also showed that the high-Z layers have a lower Mg/Fe ratio than lower Z layers (0.36 *versus* 0.40, respectively; Table 1). A microfault displaces all 5 layers, but does not cut surrounding porous oxide or fibrous phyllosilicate (Fig. 7a, b). In these multilayered bands the axial layer of Fe–Mg silicate is always parallel sided (Fig. 6), whereas the contact of flanking layers with porous oxide or fibrous phyllosilicate may be serrated (Fig. 6). Serrations can also be recognised within the Fe–Mg silicate in bright-field TEM images via subtle Z-related differences in the intensity of electron scattering (Fig. 7c, d). SAED patterns obtained from the Fe–Mg silicate contain two continuous rings with *d*-spacings of ~0.254 and ~0.155 nm. Treiman et al. (1993) also described rings in the SAED patterns with *d*-spacings of 0.25 and 0.15 nm, which they attributed to ferrihydrite. An attempt to locate the diffracting crystals by high-resolution imaging of the Fe–Mg silicate was prevented by the thickness of the foil and its susceptibility to electron beam damage.

In some of the serrated veins the Fe–Mg silicate band is flanked by selvages of porous oxide (Fig. 5). The contact between porous oxide and Fe–Mg silicate is either sharp, or gradational over the space of ~100 nm, and the profile of the interface may be straight (Fig. 7c), irregular (Figs. 4d and 7b), or serrated (Fig. 8a–c). Serrated interfaces between porous oxide and Fe–Mg silicate are observed only where the polished surface of the host olivine grain or plane of the FIB-produced foil is parallel to $(1\,0\,0)_{ol}$ (Fig. 8a, b). Teeth of porous oxide extend up to 700 nm into the Fe–Mg silicate and are symmetrical about the trace of

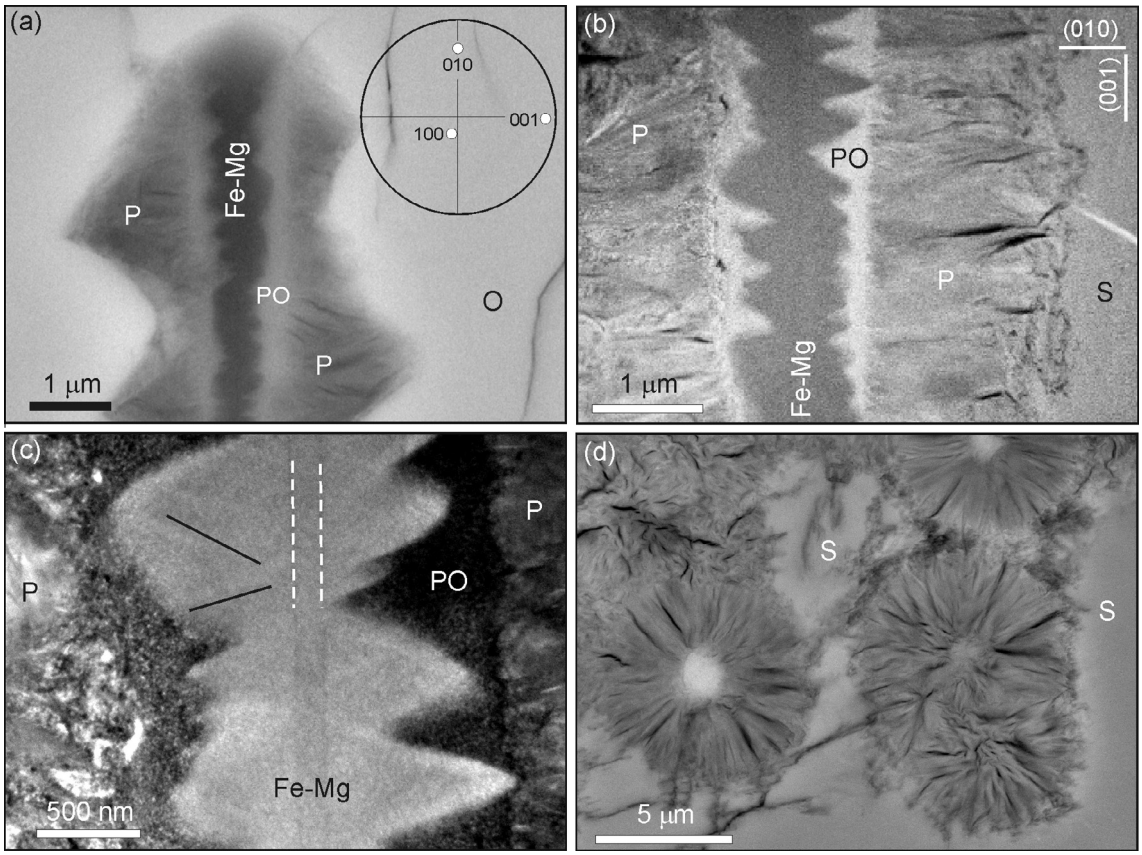

Fig. 8. Images of the fill of serrated veins showing the relationships between Fe–Mg silicate (Fe–Mg), porous oxide (PO), fibrous phyllosilicate (P), siderite (S) and olivine (O). (a) BSE image of a discontinuous finely serrated vein. The inset EBSD pole figure shows that the polished surface of the grain is close to $(100)_{ol}$, and the vein axis is parallel to the trace of $(001)_{ol}$. The vein contains an axial band of Fe–Mg silicate, which is flanked by porous oxide and fibrous phyllosilicate. The interface between porous oxide and Fe–Mg silicate is finely serrated, and the porous oxide teeth are symmetrical about the trace of $(010)_{ol}$. (b) HAADF image of a foil that was cut from a coarsely serrated olivine-hosted vein. The midplane of the foil is parallel to $(100)_{ol}$ and the orientations of the traces of $(010)_{ol}$ and $(001)_{ol}$ planes are indicated (top right hand corner). The fibrous phyllosilicate has an irregular contact with siderite and a straight boundary with porous oxide. The interface between porous oxide and Fe–Mg silicate is serrated, and the teeth are symmetrical about the trace of $(010)_{ol}$. (c) Bright-field TEM image of the upper part of the vein fill in (b). Z-related differences in the intensity of electron scattering reveal a straight-sided central band within the Fe–Mg silicate that is 150 nm wide (highlighted by dashed white lines). The Fe–Mg silicate also contains serrations (highlighted by solid black lines) that mirror the outlines of the porous oxide teeth. (d) BSE image of siderite within a coarsely serrated vein. The siderite has been partially replaced by rosettes of fibrous phyllosilicate, two of which have high-Z cores (white) that are probably composed of porous oxide.

$(010)_{ol}$ (Fig. 8b, c). Bright-field TEM images show that Fe–Mg silicate surrounding the porous oxide teeth has a faint microstructure that follows the profile of the teeth and is revealed by Z-related contrasts in the intensity of electron scattering (Fig. 8c). In a few of the veins a selvage of porous oxide lies along the centre of a Fe–Mg silicate band. TEM images of a foil cut and extracted from one of these veins show that the central porous oxide selvage is connected to a veinlet of porous oxide that cross-cuts the Fe–Mg silicate (Fig. 7c). Porous oxide veinlets cross-cutting Fe–Mg silicate have also been observed in BSE images (Fig. 5b).

Qualitative chemical analysis of porous oxide teeth by LV-STEM EDX shows they are rich in O, Si and Fe, but also have detectable C, Mg, Ca and Mn. Their chemical composition is therefore similar to Fe–Mg silicate and fibrous phyllosilicate, but the porous oxide teeth have higher C/Si, O/Si, Ca/Si, Mn/Si and Fe/Si ratios, and lower Mg/Si. The same element ratios are also greater in siderite relative to the Fe–Mg silicate and fibrous phyllosilicate. The porous oxide is polycrystalline, and constituent crystals are ~30 nm in size. SAED patterns yield rings with *d*-spacings of 0.447–0.450, 0.260–0.250 and 0.155 nm, which are similar to *d*-spacings obtained from both the Fe–Mg silicate and fibrous phyllosilicate (see below). The porous oxide has additional reflections from coarser grains whose 0.360–0.370 nm *d*-spacing of is consistent with hematite $\{01\bar{1}2\}$ ($d = 0.369$ nm) and/or siderite $\{01\bar{1}2\}$ ($d = 0.359$ nm).

Fringes of fibrous phyllosilicate 1.3–4.5 μm in width straddle the Fe–Mg silicate band in some of the finely serrated veins and all of the coarsely serrated ones (e.g., Fig. 5); individual phyllosilicate fibres may also cross-cut the Fe–Mg silicate. Where a simple vein intersects a

coarsely serrated vein the fringe of fibrous phyllosilicate is continuous between the two, although it is narrower astride the simple vein (Fig. 5b). Those coarsely serrated veins that are wider than ~10 μm (i.e., the combined width of the Fe–Mg silicate band plus flanking fibrous phyllosilicate) contain siderite (Fig. 5a–c). As described by Tomkinson et al. (2013a), this siderite formed by replacement of olivine, and the coarsely serrated contact between olivine and siderite reflects a crystallographic control on the trajectory of the replacement front. Phyllosilicate fibres may splay out into siderite from the edge of the Fe–Mg silicate band, and the contact between phyllosilicate and siderite is often finely crenulated. Veinlets and rosettes of phyllosilicate also occur within the siderite (Fig. 8d), but there is no fringe of fibrous phyllosilicate at the interface between siderite and olivine. Even though constituent fibres of the phyllosilicate are of sufficient size to resolve by BSE imaging, individual crystals are difficult to identify by TEM. SAED patterns contain rings, showing that the phyllosilicate crystals are much smaller than the ~1 μm diameter selected area aperture. The rings have *d*-spacings of 0.447, 0.253, 0.172 and 0.151 nm, and the SAED patterns may also yield spots with *d*-spacings of 0.280–0290 and 0.215 nm.

4. DISCUSSION

This study has sought to determine the origin of iddingsite veins within the Lafayette meteorite by testing two hypotheses: cementation and replacement. Only by understanding vein origins can the sequence of precipitation of the secondary minerals be established, and then broader questions about Amazonian fluid evolution be fully addressed.

4.1. Previous interpretations of vein origins

Several previous studies have concluded that the Lafayette iddingsite veins formed by replacement of olivine (Reid and Bunch, 1975; Treiman et al., 1993; Meunier et al., 2012), whereas Treiman (2005) proposed that the iddingsite filled cavities resulting from dissolution of the primary minerals. Vicenzi and Heaney (2000) and Changela and Bridges (2011) both described sequences of reactions including both cementation and replacement. Vicenzi and Heaney (2000) proposed that olivine was initially fractured by shock accompanying an impact, then iddingsite veins formed in 4 stages: (i) precipitation of siderite from low temperature solutions, the siderite being formed by replacement of fracture walls in this model; (ii) partial dissolution of siderite and precipitation of an amorphous Fe-rich silicate along the vein axis; (iii) deposition of a more Si-rich amorphous silicate on the vein axis; (iv) precipitation of phyllosilicate at the interface of the Fe-rich silicate and siderite. In a study of the nakhlites that focused on Lafayette, Changela and Bridges (2011) concluded that the olivine-hosted veins had formed in the following sequence: (i) development of sawtooth fractures by impact; (ii) crystallization of siderite on vein walls, followed by corrosion; (iii) phyllosilicate crystallization in zones within the veins and as spherical rosettes; (iv) cementation by Fe-oxide; (v) cementation by amorphous gel.

4.2. Model for iddingsite vein formation

The studies described above envisage space for the olivine-hosted veins having been formed by fracturing and/or dissolution. Pores opened up by fracturing can have developed into veins only by cementation, whereas if space were created by dissolution, the secondary minerals could have precipitated in step with a retreating olivine surface (i.e., coupled dissolution–precipitation), or filled pore space at a later time (i.e., cementation). These three possibilities for nakhlite vein formation were also recognised and discussed by Velbel (2012). Here we develop a 4-stage model that features cementation of narrow fracture pores by Fe–Mg silicate to make the augite-hosted veins and simple olivine-hosted veins, which was followed by a sequence of mineralogically and microstructurally controlled replacement reactions to make the serrated olivine-hosted veins. Further insights into the drivers of water–mineral interaction are sought by comparing and contrasting results from Lafayette with altered olivine in carbonaceous chondrite meteorites and terrestrial basalts.

4.2.1. Stage 1: Opening of narrow fracture pores in augite and olivine

All of the veins within augite grains, and many of the olivine-hosted veins, are interpreted to have formed from narrow (~1 to 2 μm wide) straight or curved pores. These pores were most likely formed by fracturing, and developed in a range of crystallographic orientations, as evidenced by their low degree of preferred orientation. Berkley et al. (1980) concluded that the nakhlites were fractured in response to impacts, which is consistent with microstructural evidence that these meteorites have been shocked to 5–14 GPa (Fritz et al., 2005). As the [0 0 1](0 1 0) dislocations in Lafayette olivine are indicative of shock to more than ~10 GPa (Langenhorst, 2002), the meteorite must have experienced pressures at the higher end of the range proposed by Fritz et al. (2005). This episode of shock may also have been responsible for the formation of low angle subgrain boundaries within olivine grains and the opening of fractures along grain boundaries.

4.2.2. Stage 2: Cementation of fracture pores by Fe–Mg silicate

At some time after fracturing, a proportion of the narrow pores within augite and olivine grains were cemented by Fe–Mg silicate (the origin of solutes needed to form this material is discussed in later sections). Identification of the constituents of the Fe–Mg silicate was not a primary goal of this study, although our observations can provide some constraints. The presence of continuous rings in SAED patterns indicates that volumes of Fe–Mg silicate sampled by ~1 μm diameter selected area apertures contain large numbers of randomly oriented nanometre sized crystals. The *d*-spacings are consistent with two-line ferrihydrite (Treiman et al., 1993; Janney et al., 2000). Given the chemical composition of pure ferrihydrite ($5Fe_2O_3{\cdot}9H_2O$), it cannot be the sole constituent of the Fe–Mg silicate. A proportion of the Mg, Si and other elements (Table 1) could be held within the ferrihydrite itself; for example, Greshake (1997)

recorded 10.4–14.1 wt.% SiO_2, up to 3.3 wt.% MgO and up to 2.3 wt.% CaO in ferrihydrite from the carbonaceous chondrite Acfer 094 (note these analyses were normalised to 100% oxide excluding water). Nonetheless, other minerals are likely to be present including saponite, which was observed within the Fe–Mg silicate by Treiman et al. (1993).

Our petrographic observations are inconsistent with an origin for the serrated veins by cementation of serrated shock-formed fractures, and the three key lines of evidence are as follows: (i) Coarsely serrated veins are commonplace in olivine grains but are absent from adjacent augite, which is very difficult to reconcile with an origin by shock fracturing; (ii) serrated fracture pores do not form during natural and experimental shock of olivine (e.g., Ashworth and Barber, 1975; Langenhorst et al., 1975, 1999); (iii) it is very rare that the notches in one wall of a serrated vein match up with teeth on the opposite wall (i.e., so that they would interlock if the vein were to close), which is a property that was used by Changela and Bridges (2011) as evidence to support vein formation by cementation of shock-formed fractures. Even if they did not form by shock, serrated pores could have been produced by dissolution of olivine. However, for the coarsely serrated veins to have formed from pores of such a size and shape they would need to have been cemented in sequence by siderite, fibrous phyllosilicate and porous oxide growing inwards from opposite walls of each pore. In every vein these cements would need to have stopped growing ~1 to 5 μm before they would otherwise have met along the axis of the pore in order to leave space for the final band of Fe–Mg silicate. Furthermore, the two crystallization fronts that were moving inwards and towards the vein axis from opposite vein walls would need to have been straight and parallel to each other regardless of the pronounced irregularity of the walls on which the secondary minerals had nucleated. We feel that it is a much better explanation that the band of Fe–Mg silicate was deposited first in narrow parallel sided fractures (i.e., stage 2), then the siderite and fibrous phyllosilicate formed sequentially by replacement of vein walls. These reactions are described in stages 3 and 4.

4.2.3. Stage 3: Incongruent dissolution of vein walls to form serrated veins

If it is assumed that all of the open fractures and the now cemented fractures (i.e., veins) within augite and olivine grains formed at the same time, then the data in Table 2 show that between 14% and 45% of the fractures in olivine were mineralized (i.e., $v_{mean} = 14–45\%$ of $v_{mean} + f_{mean}$) but only 0–30% of the augite-hosted fractures were cemented by secondary minerals. Although some of the open fractures in both minerals formed subsequent to aqueous activity, these data suggest that a greater proportion of olivine- than augite-hosted fractures developed into veins. Such a mineralogical control on vein formation is interpreted to be due to reactions between aqueous solutions and vein walls, with the olivine being substantially more reactive than augite. This widening led to the development of fine serrations on the walls of both augite- and olivine-hosted veins, and the serrations in augite are reminiscent of weathering textures in terrestrial pyroxenes (Fig 2b, c; Velbel and Losiak, 2010), and in pyroxene from the martian meteorite ALH 84001 (Thomas-Keprta et al., 2009; Velbel, 2012). Serrations are not observed on the walls of all of the olivine-hosted veins that have been widened because the teeth have the three-dimensional shape of ridges whose apices are parallel to $(0\,1\,0)_{ol}$; thus, serrations will be observed only in those veins that have been cut at low angles to $(1\,0\,0)_{ol}$. The preferred orientation of veins within both augite and olivine (Table 2) demonstrates a crystallographic control on the rate of reaction between vein walls and aqueous solutions, and only those olivine-hosted veins whose walls were parallel to (0 0 1) were widened.

The fracture pore from which the serrated veins developed is commonly preserved as a parallel-sided axial layer of Fe–Mg silicate that is typically richer in Fe than the flanking layers (e.g., Figs. 6 and 8c). The presence within veins of an axial layer with a distinct chemical composition or mineralogy is a characteristic of their formation by centripetal replacement; such veins have, for example, been documented in partially altered olivine crystals from CM2 carbonaceous chondrites (Hanowski and Brearley, 2001; Velbel et al., 2012). Further evidence for vein widening by centripetal replacement is the presence of compositional differences within bands of Fe–Mg silicate, whose serrated shape shows that they represent the former positions of retreating olivine vein walls (Figs. 6b and 7d). The characteristic teeth and notches of veins walls have formed owing to a crystallographic control on the trajectory of the replacement front. Lee et al. (2013) proposed that shock-formed [0 0 1]{1 1 0} and [0 0 1](1 0 0) dislocations contributed to the development of fine serrations on the walls of olivine-hosted veins in Nakhla (i.e., dissolution rates were locally enhanced by elastically strained crystal structure associated with the dislocations). Dislocations in Lafayette olivine grains have the same [0 0 1] Burgers vector and a comparable density, and so could have also focused dissolution along the $(0\,0\,1)_{ol}$-parallel walls of veins to generate serrations. However, as these veins are comparable in both crystallographic orientation and microstructure to olivine-hosted iddingsite veins in (presumably unshocked) terrestrial basalts, prior impact deformation may not have been essential for formation of the serrated veins in Lafayette. For example, Baker and Haggerty (1967, p. 260) found that alteration of terrestrial olivine starts along cracks perpendicular to $[0\,0\,1]_{ol}$, and further observe that "Initially a fine sawtooth pattern forms along the cracks, and later, jagged "teeth", projecting into fresh olivine are developed". Delvigne et al. (1979) and Delvigne (1998, p. 267) also observed that the replacement of olivine in basalt is initiated along cracks oriented "more or less perpendicular to the *c* axis of the olivine". A characteristic of this style of alteration is a sawtooth texture, with teeth projecting into olivine, and arranged symmetrically on both sides of the fracture. The selective alteration of basalt to form channels oriented parallel to (0 0 1) has also been recorded by TEM studies (Smith et al., 1987; Banfield et al., 1990). Smith et al. (1987) noted that iddingsite formation starts with the projection of narrow veins with wedge-shaped tips into olivine, and further breakdown leaves diamond-shaped domains of olivine delineated by {1 1 1}.

At the same time as veins were being widened, they extended in the [100]–[010] plane from (100) and (010) olivine grain boundaries, and from the tips of discontinuous veins. Extension of veins in the [100]–[010] plane was primarily achieved by growth and coalescence of {111} faceted inclusions on $(001)_{ol}$ subgrain boundaries. This control on vein formation by subgrain boundaries probably also accounts for the semi-regular spacing of serrated veins (i.e., they are exploiting similarly spaced subgrain boundaries), and the absence of serrated veins on olivine grain boundaries oriented parallel to (001). A model developed by Plümper et al. (2012) to describe the formation of serpentine veins in terrestrial olivine suggests the mechanism by which the Lafayette veins may have been widened and lengthened. They proposed that interface-coupled dissolution–precipitation on the walls of an initial fracture or etch pit produces hydrous minerals whose volumetric expansion generates stresses at etch pit corners. These stresses are sufficient to fracture the olivine, thus enabling aqueous solutions to penetrate further into grain interiors. The hairline cracks that are associated with the faceted inclusions beyond the tips of discontinuous veins in Lafayette (e.g., Fig. 4a, b) are good evidence that the precipitation of Fe–Mg silicate has fractured the olivine, thus increasing the surface area available for aqueous alteration.

4.2.4. Stage 4: Carbonation of vein walls and replacement of siderite by phyllosilicate

Following Fe–Mg silicate precipitation, the walls of many veins were replaced by siderite, and the coarse serrations that formed by this carbonation reaction are the consequence of a crystallographic control of the trajectory of the dissolution–precipitation front (Tomkinson et al., 2013a). The porous oxide is interpreted to have formed during siderite crystallization, but by non-isochemical coarsening of the Fe–Mg silicate. Cross-cutting relationships in Fig. 7b and c demonstrate that the porous oxide postdates Fe–Mg silicate (as also observed by Treiman et al., 1993), and its origin by coarsening is indicated by several petrographic characteristics: (i) the high aspect ratio of porous oxide teeth and their polycrystalline nature is inconsistent with them having grown into a void (i.e., such delicate finely crystalline structures could only have formed with support from enclosing Fe–Mg silicate); (ii) the contact of teeth with Fe–Mg silicate may be gradational, as would be expected for an origin of the porous oxide by recrystallization; (iii) the control on shape of the porous oxide teeth by the symmetry of the enclosing olivine crystal (i.e., teeth are symmetrical about the trace of $(010)_{ol}$) can be explained by a control on growth of the teeth by sub-micrometre scale compositional differences within in the Fe–Mg silicate, themselves inherited from the olivine that it has replaced. The nanocrystalline nature of the Fe–Mg silicate, and the possible presence within it of metastable ferrihydrite, could have made it especially prone to recrystallization. Coarsening of Fe–Mg silicate in the presence of the Ca–Mn–Fe–CO_2 rich solutions that precipitated the siderite is consistent with the C/Si, O/Si, Ca/Si, Mn/Si and Fe/Si ratios of the porous oxide, which are greater than in both the Fe–Mg silicate and fibrous phyllosilicate. The carrier of the C, Ca and Mn is likely to be siderite crystals, and they have been tentatively identified in the porous oxide by SAED.

Siderite was subsequently replaced by the fibrous phyllosilicate (Changela and Bridges, 2011; Tomkinson et al., 2013a), which most commonly forms a fringe straddling the Fe–Mg silicate band, but also occurs within the siderite as veinlets and rosettes. A fringe of fibrous phyllosilicate would be expected to be present at the interface between siderite and olivine, but is rarely observed. This counterintuitive finding may simply be because the siderite–olivine contact was less permeable than the interface between siderite and Fe–Mg silicate (the fractures currently present along the interface between siderite and olivine postdate secondary mineralization). The other possibility is that the fibrous phyllosilicate nucleated on the porous oxide, which is supported by the observation that fibrous phyllosilicate rosettes commonly have a porous oxide nucleus (Fig. 8d). There is no evidence for precipitation of secondary minerals after the fibrous phyllosilicate, but as the iddingsite veins are cut by open fractures, secondary mineralization was followed by an episode of deformation, which may have been in response to impact ejection of Lafayette from Mars.

4.3. Insights into the provenance and longevity of martian crustal fluids

The source of the aqueous solutions from which the Lafayette iddingsite precipitated can be inferred from the deuterium/hydrogen (D/H) ratio of water in its secondary minerals. Leshin et al. (1996) determined the D/H ratio of water liberated from two bulk samples of Lafayette by combustion and pyrolysis, and recorded a maximum δD of +896‰ ($\delta D = [(D/H)_{sample}/(D/H)_{SMOW} - 1] \times 1000$). Tomkinson et al. (2013b) obtained δD values of ~4000‰ by nanoSIMS analysis of the walls of olivine-hosted iddingsite veins. As the present-day martian atmosphere has a δD of ~5000‰ to 6000‰ (Webster et al., 2013), these D/H results are consistent with formation of the Lafayette iddingsite from a reservoir of water that was in equilibrium with the martian atmosphere.

Treiman et al. (1993) and Treiman and Lindstrom (1997) developed the first model for formation of the Lafayette iddingsite. They suggested that Lafayette was altered at less than 100 °C, and under low water/rock ratio conditions. Most of the ions for the iddingsite were interpreted to have been sourced from within the Lafayette parent rock by dissolution of olivine and mesostasis in the proportion of 45–65% to 55–35%, respectively. Although they did not describe the origin of the Fe–Mg silicate specifically, Treiman et al. (1993) noted that its composition varies with its petrographic context; for example, olivine-hosted Fe–Mg silicate contains 13.9 wt.% MgO and 4.8 wt.% Al_2O_3, whereas Fe–Mg silicate within the feldspar-rich mesostasis has 8.4 wt.% MgO and 11.9 wt.% Al_2O_3. This good correspondence between the chemical composition of the Fe–Mg silicate and its host is consistent with its formation by replacement of vein walls. However, the data in Table 1 show that the Fe–Mg silicate has lower Mg/Si, Mn/Si and Fe/Si values than olivine, and higher Al/Si and Ca/Si, thus showing that there was net export of Mg, Mn and Fe from the olivine and import of

Al and Ca, probably from the mesostasis, so that the geochemical environment was open at least on centimetre length scales. The subsequent replacement of olivine by siderite, then siderite by fibrous phyllosilicate, has been described by Tomkinson et al. (2013a), and their mass balance calculations are consistent with Treiman et al. (1993). In the model of Tomkinson et al. (2013a) the CO_2 required to form the siderite was sourced from the martian atmosphere, which agrees with the origin of Lafayette water inferred from its D/H values. The present study has not provided a definitive answer to the question of whether the Lafayette iddingsite formed from one or multiple pulses of water. However, as the transition from formation of the Fe–Mg silicate to precipitation of siderite is likely to have been in response to influx of CO_2-charged solutions, we propose the iddingsite formed in two separate events separated by an indeterminate length of time (i.e., Fe–Mg silicate first, followed by siderite, porous oxide and fibrous phyllosilicate). This idea is supported by evidence for brittle deformation of the Fe–Mg silicate prior to formation of porous oxide (Fig. 7b), and the finding that veins of porous oxide cross-cut the Fe–Mg silicate (e.g., Fig. 7c). There is good evidence for several discrete phases of mineralization in the iddingsite veins of other nakhlites such as Yamato 000593 (Tomkinson et al., 2013c).

Changela and Bridges (2011), Bridges and Schwenzer (2012) and Hicks et al. (2014) have developed a model for the evolution of the nakhlite aqueous system that was based on their inferred sequence of mineralization: (i) siderite cement; (ii) fibrous phyllosilicate cement/replacement; (iii) porous oxide cement; (iv) amorphous gel (i.e., Fe–Mg silicate) cement. In common with Treiman et al. (1993) and Treiman and Lindstrom (1997) they infer conditions of relatively low temperature and water/rock ratio. A proposed rapid cooling of the hydrothermal system is based on the assumption that the Fe–Mg silicate (amorphous gel) formed last. This scenario therefore differs from the present study in both mineralization history and the style of precipitation (i.e., predominantly cementation against predominantly replacement). Changela and Bridges (2011) suggested that water and CO_2 were liberated from crustal reservoirs by heating associated with an impact, and some of the evidence in support of their model was the opening of sawtooth fractures, which is again inconsistent with results of the present study (i.e., we have found that the sawtooth shape is the product of crystallographically-controlled replacement). We therefore conclude that the driver of iddingsite formation in Lafayette and the nakhlites remains unclear and needs further work; possibilities include melting of subsurface $H_2O + CO_2$ ices in response to an impact or volcanic event, or percolation into the lava flow/sill of CO_2-charged solutions from the planet's surface.

5. CONCLUSIONS

Iddingsite veins within the Lafayette meteorite record the presence of aqueous fluids that were in hydrogen isotope equilibrium with the atmosphere of Mars. There is evidence for two generations of solutions; the first formed the Fe–Mg silicate, whereas the second generation came after brittle deformation of the Fe–Mg silicate to precipitate the siderite-porous oxide-fibrous phyllosilicate assemblage. Characterisation of augite and olivine grains and the iddingsite veins by electron imaging and diffraction shows that the veins formed primarily by centripetal replacement, and there was a strong crystallographic and microstructural control on the nature of these dissolution–precipitation reactions. The sequence of vein formation is as follows:

1. Solutions initially gained access to the interiors of augite and olivine grains via 1–2 μm wide fractures to form a hydrous Fe–Mg silicate by cementation.
2. The walls of those olivine-hosted veins that were oriented parallel or close to $(0\,0\,1)_{ol}$ were widened by interface coupled dissolution–precipitation. The fine serrations on their walls reflect a micrometre-scale heterogeneity of the retreat rate of vein walls that may have been controlled by screw dislocations with a $[0\,0\,1]$ Burgers vector.
3. At the same time as being widened, the veins were lengthened in the $[1\,0\,0]$–$[0\,1\,0]$ plane by growth and coalescence of faceted inclusions of Fe–Mg silicate on $(0\,0\,1)$ subgrain boundaries.
4. Following introduction of a new pulse of fluids that were rich in CO_2, probably atmospherically derived, siderite replaced the walls of those olivine-hosted veins that were oriented parallel to $(0\,0\,1)$, and a crystallographic control on the trajectory of the dissolution-precipitation front produced the coarse serrations.
5. Reaction between the carbonating solutions and Fe–Mg silicate led to its non-isochemical coarsening and formation of the Fe-rich porous oxide.
6. The last of the secondary minerals to form was fibrous phyllosilicate (saponite), which replaced the siderite.

ACKNOWLEDGEMENTS

We thank Peter Chung (School of Geographical and Earth Sciences, University of Glasgow) for assistance with the SEM, and Billy Smith, Colin How and Sam MacFadzean (School of Physics and Astronomy, University of Glasgow) for help with the FIB and TEM work. We are also grateful to the Smithsonian Institution for loan of the Lafayette thin section, and to Dr Caroline Smith at the Natural History Museum (London) for loan of the meteorite sample. This research was funded by the UK Science and Technology Facilities Council (STFC) through grants ST/H002472/1 and ST/H002960/1. The manuscript has benefitted from knowledgeable and constructive reviews by Takashi Mikouchi and Michael Velbel, and we are also grateful to Wolf Uwe Reimold for editorial handling.

APPENDIX A. SUPPLEMENTARY DATA

Supplementary data associated with this article can be found, in the online version, at http://dx.doi.org/10.1016/j.gca.2015.01.022.

REFERENCES

Ashworth J. R. and Barber D. J. (1975) Electron petrography of shock-deformed olivine in stony meteorites. *Earth Planet. Sci. Lett.* **27**, 43–50.

Baker I. and Haggerty S. E. (1967) The alteration of olivine in basaltic and associated lavas. Part II: intermediate and low temperature alteration. *Contrib. Mineral. Petrol.* **16**, 258–273.

Banfield J. F., Veblen D. R. and Jones B. F. (1990) Transmission electron-microscopy of subsolidus oxidation and weathering of olivine. *Contrib. Mineral. Petrol.* **106**, 110–123.

Berkley J. L., Keil K. and Prinz M. (1980) Comparative petrology and origin of Governador Valadares and other nakhlites. *Proc. Lunar Planet. Sci. Conf.* **11**, 1089–1102.

Borg L. and Drake M. J. (2005) A review of meteorite evidence for the timing of magmatism and of surface or near-surface liquid water on Mars. *J. Geophys. Res.* **110**, E12S03.

Bridges J. C. and Grady M. M. (2000) Evaporite mineral assemblages in the nakhlite (martian) meteorites. *Earth Planet. Sci. Lett.* **176**, 267–279.

Bridges J. C. and Schwenzer S. P. (2012) The nakhlite hydrothermal brine on Mars. *Earth Planet. Sci. Lett.* **359–360**, 117–123.

Bunch T. E. and Reid A. M. (1975) The nakhlites Part 1: Petrography and mineral chemistry. *Meteoritics* **10**, 303–315.

Changela H. G. and Bridges J. C. (2011) Alteration assemblages in the nakhlites: variation with depth on Mars. *Meteorit. Planet. Sci.* **45**, 1847–1867.

Delvigne J. (1998) Atlas of micromorphology of mineral alteration and weathering. *Can. Mineral.* **3**, 495 (Special Publication).

Delvigne J., Bisdom E. B. A., Sleeman J. and Stoops G. (1979) Olivines: their pseudomorphs and secondary products. *Pédologie* **39**, 247–309.

Eugster O., Weigel A. and Polnau E. (1997) Ejection times of martian meteorites. *Geochim. Cosmochim. Acta* **61**, 2749–2757.

Friedman-Lentz R. C., Taylor G. J. and Treiman A. H. (1999) Formation of a martian pyroxenite: a comparative study of the nakhlite meteorites and Theo's Flow. *Meteorit. Planet. Sci.* **34**, 919–932.

Fritz J., Artemieva N. and Greshake A. (2005) Ejection of Martian meteorites. *Meteorit. Planet. Sci.* **40**, 1393–1411.

Gooding J. L., Wentworth S. J. and Zolensky M. E. (1991) Aqueous alteration of the Nakhla meteorite. *Meteoritics* **26**, 135–143.

Greshake A. (1997) The primitive matrix components of the unique carbonaceous chondrite Acfer 094: a TEM study. *Geochim. Cosmochim. Acta* **61**, 437–452.

Hanowski N. P. and Brearley A. J. (2001) Aqueous alteration of chondrules in the CM carbonaceous chondrite, Allan Hills 81002: implications for parent body alteration. *Geochim. Cosmochim. Acta* **65**, 495–518.

Harvey R. P. and McSween H. Y. (1992) Petrogenesis of the nakhlite meteorites: evidence from cumulate mineral zoning. *Geochim. Cosmochim. Acta* **56**, 1655–1663.

Hicks L. J., Bridges J. C. and Gurman S. J. (2014) Ferric saponite and serpentine in the nakhlite martian meteorites. *Geochim. Cosmochim. Acta* **136**, 194–210.

Janney D. E., Cowley J. M. and Buseck P. R. (2000) Transmission electron microscopy of synthetic 2- and 6-line ferrihydrite. *Clays Clay Miner* **48**, 111–119.

Jull A. J. T., Eastoe C. J. and Cloudt S. (1999) Terrestrial age of the Lafayette meteorite and stable-isotopic composition of weathering products. *Lunar Planet. Sci. 28*. Lunar Planet. Inst., Houston. #1581 (abstr.).

Karlsson H. R., Clayton R. N., Gibson, Jr., E. K. and Mayeda T. K. (1992) Water in SNC meteorites: evidence for a Martian hydrosphere. *Science* **255**, 1409–1411.

Langenhorst F. (2002) Shock metamorphism of some minerals: basic introduction and microstructural observations. *Bull. Czech Geol Surv* **77**, 265–282.

Langenhorst F., Joreau P. and Doukhan J. C. (1975) Thermal and shock metamorphism of the Tenham chondrite: a TEM examination. *Geochim. Cosmochim. Acta* **59**, 1835–1845.

Langenhorst F., Boustie M., Migault A. and Romain J. P. (1999) Laser shock experiments with nanosecond pulses: a new tool for the reproduction of shock defects in olivine. *Earth Planet. Sci. Lett.* **173**, 333–342.

Lee M. R. (2010) Transmission electron microscopy (TEM) of Earth and planetary materials: a review. *Mineral. Mag.* **74**, 1–27.

Lee M. R. and Smith C. L. (2006) Scanning transmission electron microscopy using a SEM: applications to mineralogy and petrology. *Mineral. Mag.* **70**, 561–572.

Lee M. R., Bland P. A. and Graham G. (2003) Preparation of TEM samples by focused ion beam (FIB) techniques: applications to the study of clays and phyllosilicates in meteorites. *Mineral. Mag.* **67**, 581–592.

Lee M. R., Brown D. J., Smith C. L., Hodson M. E., MacKenzie M. and Hellmann R. (2007) Characterisation of mineral surfaces using FIB and TEM: a case study of naturally-weathered alkali feldspars. *Am. Mineral.* **92**, 1383–1394.

Lee M. R., Tomkinson T., Mark D. F., Stuart F. M. and Smith C. L. (2013) Evidence for silicate dissolution on Mars from the Nakhla meteorite. *Meteorit. Planet. Sci.* **48**, 224–240.

Leshin L. A., Epstein S. and Stolper E. M. (1996) Hydrogen isotope geochemistry of SNC meteorites. *Geochim. Cosmochim. Acta* **60**, 2635–2650.

Leshin L. A. and Vicenzi E. (2006) Aqueous processes recorded by Martian meteorites: Analyzing Martian water on Earth. *Elements* **2**, 157–162.

Meunier A., Petit S., Ehlmann B. L., Dudoignon P., Westall F., Mas A., El Albani A. and Ferrage E. (2012) Magmatic precipitation as a possible origin of Noachian clays on Mars. *Nat. Geosci.* **5**, 739–743.

Mikouchi T., Miyamoto M., Koizumi E., Makishima J. and McKay G. (2006) Relative burial depths of nakhlites: an update. *Lunar Planet. Sci. 37*. Lunar Planet. Inst., Houston. #1865 (abstr.).

Mikouchi T., Makishima J., Kurihara T., Hoffmann V. H. and Miyamoto M. (2012) Relative burial depth of nakhlites revisited. *Lunar Planet. Sci. 43*. Lunar Planet. Inst., Houston. #2363 (abstr.).

Nininger H. H. (1935) The Lafayette meteorite. *Pop. Astron.* **43**, 404–408.

Plümper O., Røyne A., Magrasó A. and Jamtveit B. (2012) The interface-scale mechanism of reaction-induced fracturing during serpentinization. *Geology* **40**, 1103–1106.

Reid A. M. and Bunch T. E. (1975) The nakhlites Part II: where, when and how. *Meteoritics* **10**, 317–324.

Smith K. L., Milnes A. R. and Eggleton R. A. (1987) Weathering of basalt: formation of iddingsite. *Clays Clay Miner.* **35**, 418–428.

Thomas-Keprta K. L., Clemett S. J., McKay D. S., Gibson E. K. and Wentworth S. J. (2009) Origins of magnetite nanocrystals in Martian meteorite ALH84001. *Geochim. Cosmochim. Acta* **73**, 6631–6677.

Tomkinson T., Lee M. R., Mark D. F. and Smith C. L. (2013a) Sequestration of Martian CO_2 by mineral carbonation. *Nat. Commun.* **4**, 2662.

Tomkinson T., Lee M. R., Mark D. F., Franchi I. A. and Smith C. L. (2013b) Provenance of water in martian meteorites: D/H ratios of Lafayette using NanoSIMS (abstract). *Meteorit. Planet. Sci.* **48**, A343.

Tomkinson T., Lee M. R., Mark D. F. and Franchi I. A. (2013c) Evidence for multiphase aqueous alteration of the Yamato 00 nakhlites (abstract). *Meteorit. Planet. Sci.* **48**, A342.

Treiman A. H. (1986) The parental magma of the Nakhla achondrite: ultrabasic volcanism on the shergottite parent body. *Geochim. Cosmochim. Acta* **50**, 1061–1070.

Treiman A. H. (2005) The nakhlite meteorites: augite-rich igneous rocks from Mars. *Chem. Erde* **65**, 203–270.

Treiman A. H. and Lindstrom D. J. (1997) Trace element geochemistry of Martian iddingsite in the Lafayette meteorite. *J. Geophys. Res.* **102**, 9153–9163.

Treiman A. H., Barrett R. A. and Gooding J. L. (1993) Preterrestrial aqueous alteration of the Lafayette (SNC) meteorite. *Meteoritics* **28**, 86–97.

Velbel M. A. (1984) Natural weathering mechanisms of almandine garnet. *Geology* **12**, 631–634.

Velbel M. A. (1993) Formation of protective surface-layers during silicate-mineral weathering under well-leached, oxidizing conditions. *Am. Mineral.* **78**, 405–414.

Velbel M. A. (2012) Aqueous alteration in Martian meteorites: comparing mineral relations in igneous-rock weathering of Martian meteorites and in the sedimentary cycle of Mars. In *Sedimentary Geology of Mars* (eds. J. Grotzinger and R. Milliken). Society for Sedimentary Geology Special Publication, pp. 97–117.

Velbel M. A. and Losiak A. I. (2010) Denticles on chain silicate grain surfaces and their utility as indicators of weathering conditions on Earth and Mars. *J. Sediment. Res.* **80**, 771–780.

Velbel M. A., Tonui E. K. and Zolensky M. E. (2012) Replacement of olivine by serpentine in the carbonaceous chondrite Nogoya (CM2). *Geochim. Cosmochim. Acta* **87**, 117–135.

Vicenzi E. P. and Heaney P. J. (2000) Multiple martian fluids: the alteration sequence in the Lafayette SNC meteorite (abstract). *Meteorit. Planet. Sci.* **35**, A164–A165.

Vicenzi E. P., Tobin K., Heaney P. J., Onstott T. C. and Chun J. (1997) Carbonate in Lafayette meteorite: a detailed microanalytical study (abstract). *Meteorit. Planet. Sci.* **32**, A132–A133.

Webster C. R., Mahaffy P. R., Flesch G. J., Niles P. B., Jones J. H., Leshin L. A., Atreya S. K., Stern J. C., Christensen L. E., Owen T., Franz H., Pepin R. O. and Steele A.the MSL Science Team, (2013) Isotope ratios of H, C, and O in CO_2 and H_2O of the Martian atmosphere. *Science* **341**, 260–263.

Associate editor: Wolf Uwe Reimold